

The Distillation Curve and Sooting Propensity of a Typical Jet Fuel

Chiara Saggese¹, Ajay V. Singh¹, Xin Xue², Carson Chu³, Mohammad Reza Kholghy^{3,8}, Tongfeng Zhang³, Joaquin Camacho^{1,9}, Jennifer Giaccai⁴, J. Houston Miller⁴, Murray J. Thomson³, Chih-Jen Sung², Hai Wang^{1*}

¹Mechanical Engineering Department, Stanford University, Stanford, CA 94305, USA

²*Department of Mechanical Engineering, University of Connecticut, Storrs, CT 06269, USA*

³Department of Mechanical and Industrial Engineering, University of Toronto, Toronto, Canada

⁴Department of Chemistry, The George Washington University, Washington, DC 20052, USA

*Corresponding Author: haiwang@stanford.edu

⁸Current address: Department of Mechanical and Process Engineering, ETH Zurich, Switzerland

[#]Current address: Department of Mechanical Engineering, San Diego State University, San Diego, CA 92182, USA

Abstract

Real jet fuels are complex mixtures of many organic components, some of which are aromatic compounds. Towards the high-temperature end of the distillation curve, some of the fuel components are multi-ring compounds. A small amount of these high molecular weight species in the fuel could impact soot nucleation in practical engines especially when the fuel is injected as a spray. This work aims to highlight the variation of the sooting propensity of jet fuels as a function of distillate fractions and to examine the validity of a surrogate fuel in emulating soot production from real fuels. Particle size distribution functions and soot volume fractions are studied in a series of laminar premixed stretch-stabilized ethylene flames doped with Jet A, its various distillate fractions, and the 2nd generation MURI surrogate. Soot formation as a result of doping real jet fuel and its distillate fractions is also investigated in counterflow and coflow diffusion flames. The results show that the higher-boiling distillates mostly influence soot nucleation and produce substantially more soot in nucleation controlled flames than the light molecular fraction and jet fuel as received, while such an effect is seen to be small in flames where soot production is controlled by surface growth. The potential impact of distillate fractions on soot nucleation propensities is discussed.

Keywords:

Jet fuel, Flame; Soot; Particle size distribution; Distillation curve

33 1. Introduction

34 Conventional jet fuels are of a distillate origin of crude oils and multicomponent in nature. A
35 typical jet fuel may contain thousands of hydrocarbon compounds [1-3], among which up to \sim 20%
36 (wt) can be aromatics [1]. The distillation curve of typical jet fuels gives hints about the presence of
37 high molecular weight species in the fuel, some of which are polycyclic in nature [4-6]. For a typical
38 Jet A, the temperature at the 90% distillation volume is around 250 °C [4], which exceeds the boiling
39 point of naphthalene (218 °C) and tetralin (208 °C). The impact of multi-ring species on soot
40 formation is apparent through a range of previous studies of soot formation, most of which were
41 conducted in counterflow or coflow diffusion flames [7-18]. In many of these studies, gaseous-
42 fueled baseline flames were doped with low concentrations of vaporized liquid jet fuels and their
43 surrogates, demonstrating the effects of dopant chemical composition on sooting tendencies while
44 preserving the main properties of the baseline flames (e.g. temperature, velocity) [11, 13-16, 18].
45 With the motivation to identify simple surrogates capable of reliably predicting the sooting behavior
46 of kerosene, Moss and Aksit [7, 12] conducted an experimental investigation on the sooting, laminar,
47 and turbulent coflow flames of aviation kerosene and blends of *n*-decane with a range of alkyl-
48 substituted aromatics. The sooting behavior of the surrogates was also compared on the basis of the
49 measured smoke points. They found that a mixture of 30% (mass) mesitylene or propylbenzene and
50 70% (mass) *n*-decane represents the sooting behavior of an aviation kerosene well in both laminar
51 and turbulent flames. Saffaripour et al. [8] studied coflow diffusion flames of pre-vaporized Jet A-1
52 and four synthetic jet fuels to compare their sooting characteristics and flame structures. They
53 showed that soot levels along the centerline of coflow diffusion flames are strongly correlated to the
54 aromatic content of the fuel, and soot and acetylene concentrations are not proportional to each
55 other. In more recent studies, Saffaripour and coworkers [9, 10] measured soot volume fraction in a
56 Jet A-1 coflow diffusion flame and compared it with the volume fraction observed in a
57 corresponding flame burning a surrogate that is comprised of 69% (mol) *n*-decane, 20% *n*-
58 propylbenzene and 11% *n*-propylcyclohexane [19]. They found that such a surrogate underpredicts
59 the soot concentrations of the real Jet A-1 up to a factor of five, and the same trend was observed in

60 the smoke points of these fuels. Consequently, they suggested that the addition of two-ring
61 aromatics is necessary in order for the surrogate to reproduce the sooting propensity of the real Jet
62 A-1. In the work of Witkowski et al. [11], soot volume fraction and morphology measurements were
63 made in a laminar coflow methane-air diffusion flame seeded with approximately 2200 ppm of a real
64 Jet A and the first-generation MURI surrogate [20] in which the aromatic component is represented
65 by 24% by volume of toluene. The surrogate jet fuel was shown to have notably lower soot volume
66 fractions than the real Jet A. In the work of Lemaire et al. [21], soot volume fraction in turbulent
67 diffusion flames burning kerosene and its surrogate was measured and compared. It was shown that
68 a surrogate containing decalin, a two-ring compound, is required to reproduce the sooting behavior
69 of real jet fuels.

70 The evolution of main oxidation products and soot precursors in methane and ethylene flames
71 doped with small amounts of jet fuel and surrogate mixtures was extensively studied also in
72 counterflow flames [14-16, 18]. For example, Honnet et al. [17] measured soot volume fraction in
73 laminar non-premixed flows burning a JP8 and the Aachen surrogate comprised of 80% *n*-decane
74 and 20% 1,2,4-trimethylbenzene by mass. They found that the Aachen surrogate reproduces the
75 sooting tendency of JP-8 well within the range of the flame conditions studied.

76 As discussed above, surrogate fuels have become a widely used approach for dealing with the
77 challenges of modeling real fuels. Most of the studies on jet fuels aimed at formulating surrogate
78 mixtures capable of reliably predicting chemical and physical properties of common aviation fuels,
79 such as volatility, boiling point curves, smoke point, advanced distillation curves, average molecular
80 weight, H/C ratio, the derived cetane number, and the threshold sooting index (TSI) [22]. Dooley et
81 al. [23] utilized the TSI, along with the average fuel molecular weight, H/C ratio, and derived cetane
82 number, as targets to match a 4-component surrogate to a target Jet A fuel (POSF 4658). The
83 components of the surrogate were blended in proportions, which minimizes the difference in the
84 aforementioned targets between the fuel and its surrogate. The performance of the surrogate was
85 compared to the real fuel in several controlled combustion experiments, including a wick-fed
86 laminar diffusion flame, which was used to measure the smoke points of the fuel and surrogate.

87 Additionally, soot volume fractions in the flame were quantified using laser light extinction; the peak
88 of volume fraction values was found to be comparable for the Jet A fuel and the surrogate at their
89 respective smoke points.

90 The aromatic content of a fuel is an important practical indicator of its sooting tendency [24].
91 This has motivated attempts to match the proportion and distribution of aromatics between a real
92 fuel and its surrogate as a way to ensure a wide range of applicability of the fuel surrogate.
93 Importantly, it has been noted that the sooting tendency of real fuels correlates well with their
94 aromatic content as long as the ratio of polyaromatics/monoaromatics is similar between the real
95 fuel and the surrogate. In a recent work [25], sooting tendencies of several jet fuels and their
96 surrogates were experimentally measured in terms of the Yield Sooting Indices (YSIs). It was found
97 that while the sooting behavior of a fuel is largely dependent on the aromatics present in the fuel, a
98 lumped parameter such as the aromatics volume percent can be inadequate for predicting the fuel
99 sooting tendency. To develop surrogates with fidelity to mimic the sooting behavior of real fuels, it
100 is important to characterize the nature of their aromatic content.

101 We wish to point out here a simple fact that has not received sufficient attention in earlier
102 studies, namely the role of the real-fuel distillation curve in soot formation. As observed in the work
103 of Bruno and coworkers [4], there is a continuous drop in the content of one-ring aromatics and a
104 simultaneous increase in the content of the two-ring aromatic compounds towards the high boiling-
105 point fractions. The very tail end of the distillation curve can reach a temperature as high as 350 °C,
106 which is in the range of the boiling points of high-molecular weight, three to four-ring aromatics
107 (e.g., 340 °C for phenanthrene and 378 °C for pyrene). Obviously, these multi-ring compounds
108 within the fuel are trace species but they still could shortcut the growth process of polycyclic
109 aromatic hydrocarbons (PAHs) and in this way, induce soot nucleation in engines especially in non-
110 premixed spray combustion. Currently, the composition of the tail end of the distillation curve is not
111 well known, as available distillation curve studies typically stop at 90% volume fraction. A range of
112 questions thus arise:

113 1) What is the nature of the fuel compounds in the tail end of the distillation curve and what role do
114 they play in soot formation?

115 2) Jet fuels are utilized in practical systems as a spray, and the distillation curve must impact, at least
116 in some cases, the local concentrations of the different constituents of the multicomponent fuels.
117 Hence, can the sequential evaporation of the fuel components, from low to high boiling points,
118 produce transient, spatial enrichment of multi-ring fuel components, thus impacting soot
119 nucleation and growth?

120 The current work aims to address a range of related questions surrounding the effect of the
121 likely existence of multi-ring species on soot formation from real jet fuels. We carry out our studies
122 across three laboratory flame platforms, from laminar premixed stretch-stabilized flames to the
123 counterflow and coflow diffusion flames. One of our emphases was to examine the sooting
124 properties of different distillate fractions of a typical Jet A. A comparison of the sooting properties
125 of the Jet A and the 2nd generation MURI surrogate (40% *n*-dodecane, 29% *iso*-octane, 7% 1,3,5-
126 trimethylbenzene and 23% *n*-propyl benzene by mole) [23] is also presented and discussed to shed
127 light on the above questions.

128

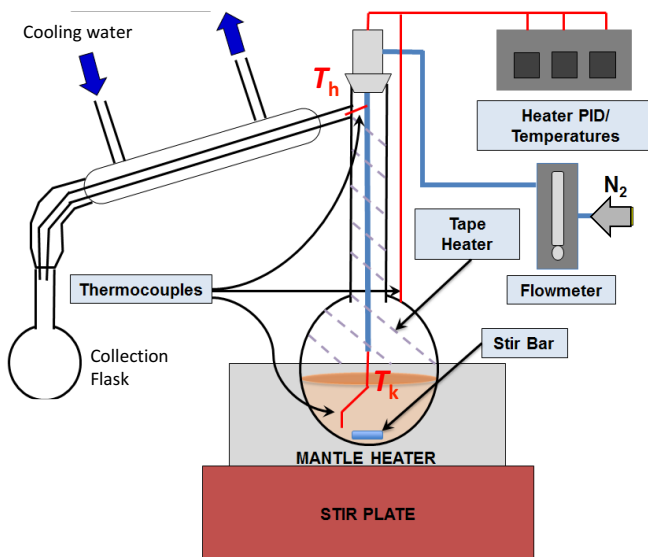
129 2. Methodology

130 2.1 Distillation setup

131 The fuel investigated in this study is an average commercial Jet A, designated as POSF 10325 [1],
132 which is basically POSF 4658 [4, 6]. In order to understand the impact of the different distillation
133 fractions on the sooting property, a range of the distillate fractions was obtained by distillation. The
134 setup and procedure follow that of Bruno and coworkers [4-6] with small modifications to ensure
135 reliable output in the volume fraction range of 90 to 100%. As depicted in Fig. 1, a round-bottom
136 flask was filled initially with 400 ml of Jet A. The liquid was stirred and heated from room
137 temperature to 360 °C using a temperature controller. In earlier distillation experiments [26, 27],
138 both N₂ and Ar were used to prevent fuel oxidation, with Ar providing somewhat better results. In
139 our measurements, a flowrate of 0.4 SCFH of N₂ was used for purging the flask from the onset of

140 heating and maintaining an inert environment, even though Ar may be more effective than N₂.
141 Vaporized fuel passes through the distillation head, condenses in a water-cooled glass Graham
142 condenser, and is collected in a calibrated flask, in which the volume measurement is made.
143 Thermocouples were used to measure the boiling flask (kettle) temperature (T_k , the liquid
144 temperature) and the head temperature (T_h , the temperature of the vapor at the bottom of the
145 takeoff position in the distillation head). The temperatures were recorded at each of the
146 predetermined distillate volume fractions. The one-standard deviation in T_k fluctuation was
147 approximately 0.6 °C, and that in T_h was approximately 3 °C. The actual uncertainty in T_h is larger
148 than 3 °C, of course, due to the difficulty in placing the thermocouple in the exact same location in
149 the distillation head. Other factors include turbulence, uniformity of vapor flow and radiative
150 heating from the glass.

151



152
153

Figure 1. Schematic diagram of the distillation setup.

154 Jet A was distilled first into 8 distillate volume fractions (0-60%, 60-70%, 70-75%, 75-80%, 80-
155 85%, 85-90%, 90-95% and 95-100%). The last fraction was distilled further, thus obtaining three
156 separate distillate (95-97.5%, 97.5-98.75%, 98.75%-100%). The density of each fraction was
157 measured and the composition was analyzed using gas chromatography-mass spectrometry (GC-
158 MS). The molecular weight (MW) and hydrogen-to-carbon (H/C) ratio were empirically estimated

159 according to the dependence of MW and H/C ratio on density among several jet fuels (see Fig. S1
160 of the Supplementary Materials):

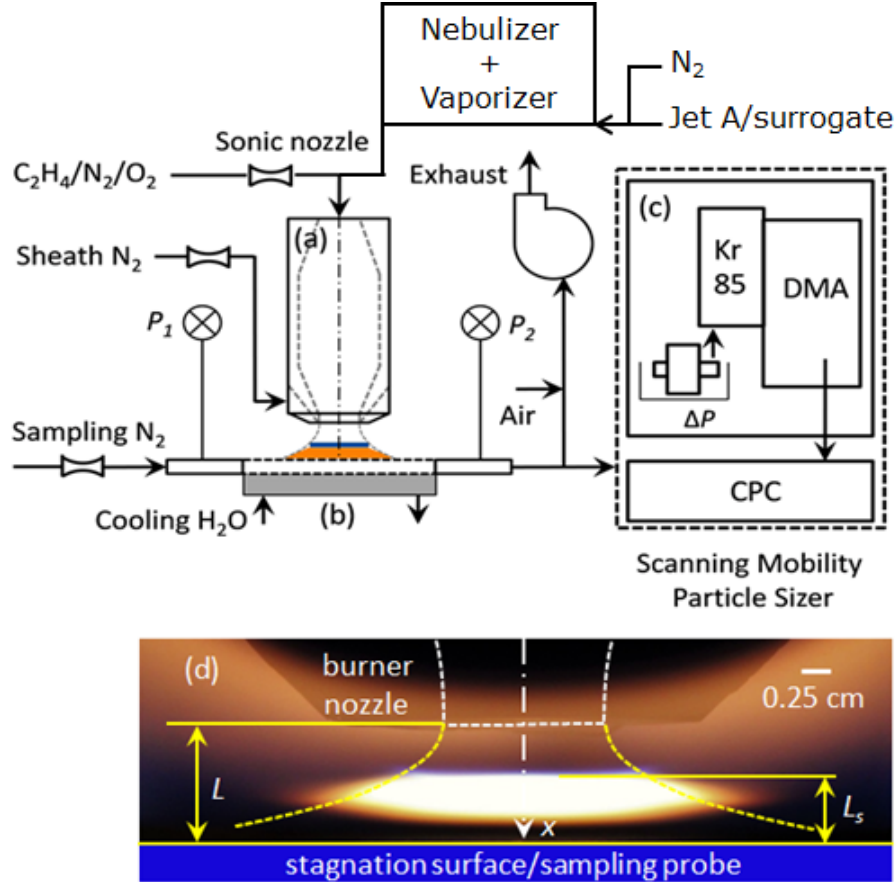
$$161 \quad \text{MW (g/mol)} = 450.97 \rho^2 - 422.58 \rho + 207.14$$

$$162 \quad \text{H/C} = 38.545 \rho^2 - 64.494 \rho + 28.845$$

163 where the density ρ is in g/cm³. The above equations are valid for $0.78 \leq \rho \text{ (g/cm}^3\text{)} \leq 0.827$.

164 *2.2 Premixed stretch-stabilized flame*

165 Setup of the premixed stretch-stabilized stagnation flame is based on the setup introduced in a
166 previous work [28] with the difference being the addition of a fuel vaporization system. As shown
167 in Fig. 2, the burner is comprised of an aerodynamically shaped nozzle, 1.43 cm in exit diameter, a
168 stagnation surface/sampling probe assembly and a scanning mobility particle sizer (SMPS). The
169 aerodynamic shape of the burner nozzle body was designed to achieve a plug flow at the burner exit.
170 The distance between the burner nozzle and stagnation plate, L , was held constant at 1.0 cm. The
171 standing distance between the flame and the stagnation surface/sampling probe, L_s , and hence the
172 reaction time beyond soot nucleation is varied by changes in the unburned gas velocity.
173



174

175 **Figure 2.** Schematic showing various parts of the experimental setup. (a) Burner nozzle, (b) sampling
 176 probe/stagnation surface, (c) Scanning Mobility Particle Sizer (SMPS), (d) a typical image of Jet A doped
 177 flame (adapted from ref. [28]).

178

179 Similar to the burner-stabilized stagnation flame sampling technique [29, 30], the water-cooled
 180 stagnation surface also acts as a sampling probe. The temperature at the stagnation surface, T_s , is
 181 measured by a type-K thermocouple placed flush with the surface such that the bead is exposed to
 182 the sample gas at a radial distance of 1 cm from the centerline of the flame. The stagnation surface
 183 temperature is $T_s = 368 \pm 25$ K for all flames tested herein. The gas temperature at the nozzle exit T_n
 184 was also determined by a type-K thermocouple and is 513 ± 10 K for all flames studied. The
 185 uncertainty values quoted here are one standard deviation.

186 Soot mobility particle size distribution functions (PSDFs) were measured at the stagnation
 187 surface on the center axis of the flame. A micro-orifice (127 μm diameter, 125 μm wall thickness)
 188 embedded within the stagnation plate continuously draws a particle-laden gas flame sample, which is

189 quickly diluted by a flow of cold nitrogen thus quenching the reaction and preventing particle losses
190 by coagulation. An optimum dilution ratio (DR) was determined following the procedure of
191 previous studies [28, 29]. The ratio was held constant for each flame (DR~10³). Mobility PSDFs are
192 determined by an SMPS (TSI 3080). Corrections for multiple charges and diffusion loss were made
193 within the Aerosol Instrument Manager software. The size of particles smaller than 10 nm can be
194 overestimated by the software due to the limitation of Cunningham slip correction [31]. The
195 mobility diameter was corrected by the relationship as discussed in [32] on the basis of an improved
196 transport theory [33,34]. In these stretch-stabilized premixed flames, nascent soot particles, as
197 defined in [35], are probed.

198 Three series of host flames (*a*, *b* and *c* as shown in Table 1) were examined for each jet fuel
199 tested, varying the unburned gas velocity while keeping all other flame parameters constant. The
200 variation in the unburned gas velocity has the effect of changing the flame standoff distance, and
201 thus it impacts the particle residence time in the flame [28]. The host flames are all near-sooting
202 ethylene-oxygen-nitrogen flames (12.2% C₂H₄, 17.8% O₂, and 70% N₂, $\phi = 2.06$) in which a given
203 liquid fuel is doped into the unburned mixture at two levels of dopant concentrations (series *i* and
204 *ii*). The liquid fuels tested are Jet A as received, its light distillate fraction from 0 to 60% and the
205 residue distillate fraction from 95 to 100%, and the 2nd generation MURI surrogate [23]. A limited
206 number of experiments were carried out also for the 98.75-100% distillate fraction. Because the
207 H/C ratios of the liquid fuel tested, including the 98.75-100% distillate fraction, are not significantly
208 different from each other, as will be discussed later, the equivalence ratio of the unburned mixture
209 stays the same at a given mass doping of the liquid fuel. These are $\phi = 2.18$ at 7260 ppm and $\phi =$
210 2.24 at 11500 ppm mass doping. The various flame parameters and the jet fuel dopants studied are
211 summarized in Table 1. The flames are labeled by “host flame series”-“liquid fuel”-“dopant mass
212 fraction series.” For example, *a*-Jet A-*i* refers to a doped flame that has a cold gas velocity of 50.3
213 cm/s (see Table 1), with Jet A as received as a dopant at a concentration of 7260 ppm by mass; *c*-
214 (95-100%)-*ii* refers to a doped flame that has a cold gas velocity of 39.7 cm/s, with the 95-100%
215 distillate fraction as a dopant at a concentration of around 11500 ppm by mass.

216 Liquid fuel was metered using a syringe pump (Harvard PHD2000), vaporized at 483 K, and
 217 mixed with the remaining gas components, as described in Ref. [36]. All unburned gas lines were
 218 maintained at 483 K and the burner temperature was set at 513 K. The nitrogen sheath flow velocity
 219 matches the cold, unburned gas velocity for each flame to minimize flame edge effects [28].

220 The premixed stretch-stabilized flame is pseudo-one dimensional and amenable to numerical
 221 simulation [28]. We used OpenSMOKE++ [37] for this purpose, with the boundary conditions
 222 appropriate for the underlying problem. The HyChem Jet A reaction model [2, 38] was used to
 223 describe the reaction kinetics of Jet A.

224
 225 **Table 1.** Flame parameters of the stretch-stabilized premixed flames, and physical properties of the
 226 jet fuels or surrogate used as the dopants (ρ : liquid mass density, MW: mean molecular weight).

Dopant	Cold gas velocity, ^a v_o (cm/s)		Host-flame unburned gas mole %		
	series <i>a</i> 50.3	series <i>b</i> 45.2	series <i>c</i> 39.7	C ₂ H ₄ 12.2%	O ₂ 17.8%
Jet A					
as received	0.803	158.6	7260 \pm 5	11490 \pm 15	
0-60% fraction	0.786	153.5	7260 \pm 9	11490 \pm 9	
95-100% fraction	0.818	163.1	7260 \pm 7	11490 \pm 11	
98.75-100% fraction	0.824	165.1	-	11500 \pm 9	
2 nd gen surrogate ^c	0.758	138.7	7260 \pm 15	11510 \pm 45	

227 ^a STP condition (298 K, 1 atm). The cold gas velocity includes the contribution from the liquid dopant. The
 228 temperature of the unburned gas is maintained at 513 \pm 10 K, and that of the stagnation surface is 368 \pm 25 K.

229 ^b Mass doping in the unburned mixture. The overall equivalence ratios are $\phi = 2.18$ (series *i*) and $\phi = 2.24$ (series *ii*).

230 ^c The surrogate is composed of 40% *n*-dodecane, 29% *iso*-octane, 7% 1,3,5-trimethylbenzene and 23% *n*-propyl
 231 benzene by mole [23].

232

233

234 2.3 Non-premixed counterflow flame

235 A counterflow burner facility was employed to study soot formation in non-premixed flames
 236 [39-41]. This facility consists of two aerodynamically converging opposing nozzles 1.0 cm in exit
 237 diameter. The nozzle to nozzle separation distance is 1.1 cm. The fuel and oxidizer streams were

238 both diluted with nitrogen. Liquid jet fuel or one of its distillates was injected using a liquid pump
239 with 0.5% accuracy and vaporized in an annular coflow of nitrogen at 503 K in a vaporization
240 chamber. Both the fuel and oxidizer streams were maintained at $T_u = 400$ K to prevent fuel
241 condensation.

242 Soot volume fraction (f_v) was measured by laser induced incandescence (LII) calibrated with light
243 extinction measurement [39-41]. The light extinction measurements used a He-Ne laser and a
244 refractive index value of $m = 1.57 - 0.56i$, a value widely adopted in the literature and also validated
245 for various flames burning different fuels [39]. The corresponding $E(m)$ value is 0.26. In the LII
246 measurement, an Nd:YAG laser (Continuum Powerlite 8010) with 10 Hz repetition rate provides a
247 532-nm laser beam, from which a laser sheet was formed by expanding it with a cylindrical plano-
248 concave lens of 2.57 cm in focal length and a plano-convex lens of 25.0 cm. The energy distribution
249 in the laser sheet is uniform due to the large vertical expansion; and the laser fluence is 0.58 J/cm².
250 An iris was also used to let the central part of the laser sheet pass through the flame. The LII signal
251 was detected at 450 nm by a Peltier cooled intensified CCD camera (Princeton Instrument, PIMAX-
252 3). The detection wavelength was selected to avoid/minimize the interference from the C₂ Swan
253 band emissions [42]. A delay of 25 ns was applied to the intensifier, corresponding to a 5 ns delay
254 from the peak LII signal, to mitigate the interference of PAH fluorescence, while a gate width of 80
255 ns was selected to avoid the particle size bias in the LII signal. The standard deviation in the LII
256 measurement was less than 18% based on 60 LII images.

257 The test conditions are shown in Table 2. The host counterflow diffusion flames were
258 established with a fuel stream of C₂H₄/N₂ flowing against an oxidizer stream of O₂/N₂. The global
259 strain rate was maintained at $K = 200$ s⁻¹, thus keeping the characteristic residence times experienced
260 by the reactants in the combustion zone the same across all test conditions. The mole fraction of
261 C₂H₄ in the fuel stream, X_F , and the mole fraction of O₂ in the oxidizer stream, X_{O_2} , were kept equal.
262 There are three series of flames (*a*, *b* and *c* as shown in Table 2): two sooting conditions, $X_F = X_{O_2} =$
263 0.40 and $X_F = X_{O_2} = 0.35$, and one near-sooting condition of $X_F = X_{O_2} = 0.30$, which were selected
264 for the host flames. Jet A or a certain distillate fraction was doped into the fuel stream at the

265 concentration of 2000 ppm by mole. In the doped flames, the ethylene mole fraction was slightly
266 reduced and accordingly to keep the total fuel mole fraction and thus the total fuel jet velocity the
267 same between the doped and host flames. The mass fractions of the doped jet fuel differ somewhat
268 because of the difference in the fuel molecular weight. The stoichiometric mixture fraction (Z_{st})
269 values of the three host flames and the doped flames are all around 0.24, indicating the similar flame
270 location for all tested conditions.

271
272
273

Table 2. Parameters of the counterflow diffusion
flames.^a

Host flame composition: $X_F = X_{O_2}$		
	0.40	0.35
	0.30	
Dopant concentration (ppm) ^b		
Jet A dopant	mole	mass
as received	2000	11330
0-60% fraction	2000	10960
95-100% fraction	2000	11650

274 ^a Nitrogen as the balance gases in both fuel and oxidizer jets at
275 400 K. All flames are at a global strain rate of 200 s⁻¹.

276 ^b Concentration in the fuel stream.

277
278

279 2.4 Non-premixed coflow flame

280 A co-annular burner assembly was used to produce atmospheric pressure laminar co-flow
281 diffusion flames [43]. Briefly, the burner consists of an inner tube 1.09 cm in inner diameter (ID),
282 0.09 cm in wall thickness, and a concentric 9 cm ID annulus for the oxidizer flow. We use ethylene
283 diluted in nitrogen to establish the host flame and air as the oxidizer flow. Jet fuel or its distillate is
284 added to the ethylene-nitrogen jet in doped flames. A syringe pump (Harvard PHD Ultra) was used
285 for liquid fuel delivery. The liquid fuel was vaporized by the Bronkhorst CEM Liquid Delivery
286 System into a nitrogen stream, which is then mixed with ethylene downstream of the vaporizer. The
287 fuel mixture was conveyed by a heated tube at 541 K to prevent condensation. The flame conditions
288 are presented in Table 3. Images of the flames are presented in Fig. S3 of the Supplementary
289 Materials.

290 Spectral Soot Emission (SSE) measurements [44] were made to obtain the flame temperature, as
 291 described in Ref. [43]. A Princeton Instrument SP2105i spectrometer accompanied by PIXIS100
 292 digital camera was used to capture the local spectral radiance collected by an optical assembly
 293 consisting of an achromatic lens with a fixed focal length of 10.0 cm and an iris with an aperture of
 294 0.2 cm. The temperature was then obtained from recovering local property fields using the Abel
 295 Inversion via the Nestor-Olsen Algorithm [45]. The absorption coefficient, $E(m)$, was assumed to be
 296 a constant and equal to 0.26 [44] for the wave length range of 491.8 to 994.8 nm used in the SSE
 297 measurements.

298 A modified Artium LII-200 time-resolved LII system, as described in [43], was used to obtain
 299 local soot volume fraction (f_s) and soot primary particle diameter (D_p). The system has an Nd-YAG
 300 laser centered at the wavelength of 1064 nm. Soot volume fraction measurements are made at a
 301 fluence of 0.1 J/cm². The LII system has default values of 0.4 for $E(m)$ and 0.26 for the thermal
 302 accommodation coefficient, α_r . The latter is needed for interpreting the LII measurements in terms
 303 of particle diameter. Soot volume fraction (f_s) can be computed from the peak soot temperature and
 304 D_p can be estimated from the temporal decay of the soot temperature to the flame temperature,
 305 which was obtained separately by the SSE as described earlier. The method to determine particle
 306 diameter is only sensitive to mature soot particles with solid appearance with primary particle
 307 diameter as small as 10 nm.

308
 309

Table 3. Non-premixed coflow flame conditions.

	Host flame	Doped flames ^a
Inner fuel flow		
C ₂ H ₄ , L/min ^b (g/hr)	0.19 (13.0)	0.17 (11.4)
Liquid fuel, g/hr		1.7
Diluent N ₂ , L/min ^b	0.5	0.5
Outer oxidizer flow (L/min)^b		
	60	60

310 ^a The dopants are jet A as received, its 0-60 % and 95-100 %
 311 distillation fractions. ^b STP condition of 298 K and 1 atm. The
 312 unburned fuel-nitrogen jet is maintained at 541 K.
 313

314 The SSE temperature measurements are subject to two sources of errors: emission attenuation
315 and background radiation. The basic theory of SSE assumes that emission attenuation can be
316 neglected [44]. However, this can be an issue in the core region of flames with strong annular soot
317 profiles, whereas the impact of emission attenuation is insignificant in the annulus regions.
318 Background radiation is more likely to be significant at locations where the local emission-to-peak
319 local emission is small [46]. Thus it is believed that, for soot profiles that are strongly annular, the
320 core region and the outer edge of the annulus are more sensitive to background radiation. In the
321 current study, since the local emission in the core region is still strong, the background radiation is
322 insignificant. However, in the outer region of the annulus ($r > r_{T_{\max}}$), the measurements are strongly
323 influenced by background radiation and therefore are ignored. The SSE technique may also suffer
324 from the errors induced by the inversion algorithm. In highly annular soot profiles, the Abel
325 Inversion causes noises in the temperature profile in the core region. In these cases, the
326 measurements in the core region are therefore ignored. In general, in the regions where sufficient
327 soot is present, the temperature measurements by the SSE technique agree well with other
328 measurement techniques such as coherent anti-Stokes Raman scattering (CARS) and rapid
329 thermocouple insertion (RTI) [44, 46].

330 It is known that $E(m)$ is subject to some uncertainty. In these measurements, the $E(m)$ values are
331 chosen to be 0.4 for LII and 0.26 for SSE. The difference is due to the difference in soot maturity,
332 with mature soot having higher $E(m)$ values. LII heats and anneals soot [43, 50], causing the
333 graphitization of soot [43, 50] and thus a higher $E(m)$ value. The value chosen is close to the upper
334 end of the $E(m)$ range (0.15 ~ 0.41) known for soot particles [47-49].

335 The reproducibility of the data was investigated. Single-shot variation was greatly reduced by
336 averaging approximately 500 single-shot measurements at each location. The measurements at each
337 location will also vary day to day because of small errors in the positioning and flow systems. This
338 repeatability was evaluated by calculating the 95% confidence interval for the distance from the
339 mean using a paired t test. Thus, the repeatability was calculated to be within ± 0.03 ppm for the
340 soot volume fraction based on 102 pairs of different day measurements. The repeatability was

341 calculated to be within ± 0.27 nm for the soot primary particle diameters (D_p) based on 44 pairs of
342 different day measurements. These repeatability intervals are shown as the error bars on the figures.
343 Another possible source of error in the D_p value could be caused by the fact that its estimation relies
344 heavily on particle specific surface area available for conduction, which does not account for size
345 distribution and particle aggregation [51]. The shielding and bridging effects, which refer to the
346 hidden primary particles inside soot aggregates and bridges among primary particles, may also
347 contribute to the error [43, 51]. The absolute errors are mainly attributed to the choice of $E(m)$. It is
348 possible that there are variations in the optical properties of the soot with flame location and
349 different fuels; a quantitative knowledge of this variation is currently unknown. However, as fuels
350 were compared under the equal settings, we believe that this uncertainty will not significantly affect
351 our conclusion.

352 During the experiment, f_r along the centerline of each flame was measured and the height that
353 produces the maximum centerline f_r , denoted as $HAB_{f_r,\max}$, was identified for each flame. The
354 $HAB_{f_r,\max}$ values are 4.8 cm for the host flame, and 5.5 cm, 5.6 cm, and 5.4 cm for flames doped with
355 Jet A as received, its 0-60% distillate fraction and 95-100% distillate fraction, respectively. Selected
356 radial temperature profiles can be found in Fig. S4 of the Supplementary Materials.
357
358

359 3. Results

360 We focus the discussion on the stretch-stabilized premixed flames first with two related
361 components: evaluating the accuracy of the 2nd generation MURI surrogate in reproducing the
362 detailed sooting properties of the Jet A tested and examining the variation of the sooting tendency
363 with respect to Jet A distillation fractions. To shed light on the second component of the study, the
364 dependency of sooting tendency on Jet A distillation fractions is further studied in laminar diffusion
365 flames in the counterflow and coflow configurations.

366 3.1 Stretch-stabilized premixed flame structures

367 Axial velocity and temperature profiles computed for the host ethylene flames doped with Jet A
 368 are shown in the top panel of Fig. 3. The maximum temperatures are all around 1900 K in host
 369 flames *a*, *b* and *c*. The preheat zone of the flame is not attached to the burner, which is typical for
 370 stretch-stabilized flames. Rather, the rise in temperature occurs where the local flow velocity
 371 approaches the laminar flame speed of the underlying unburned mixture. The variation in the
 372 unburned gas velocity corresponds to changes in the global strain rate of the flame, which in turn
 373 causes the flame standing distance and the particle residence time to vary within each series of the
 374 flame [28]. The flame structure is similar across the range of the cold gas velocity used. As an
 375 example, numerical solution of selected major and minor species of Flame *c*-Jet A-*i* is shown in the
 376 bottom panel Fig. 3.

377

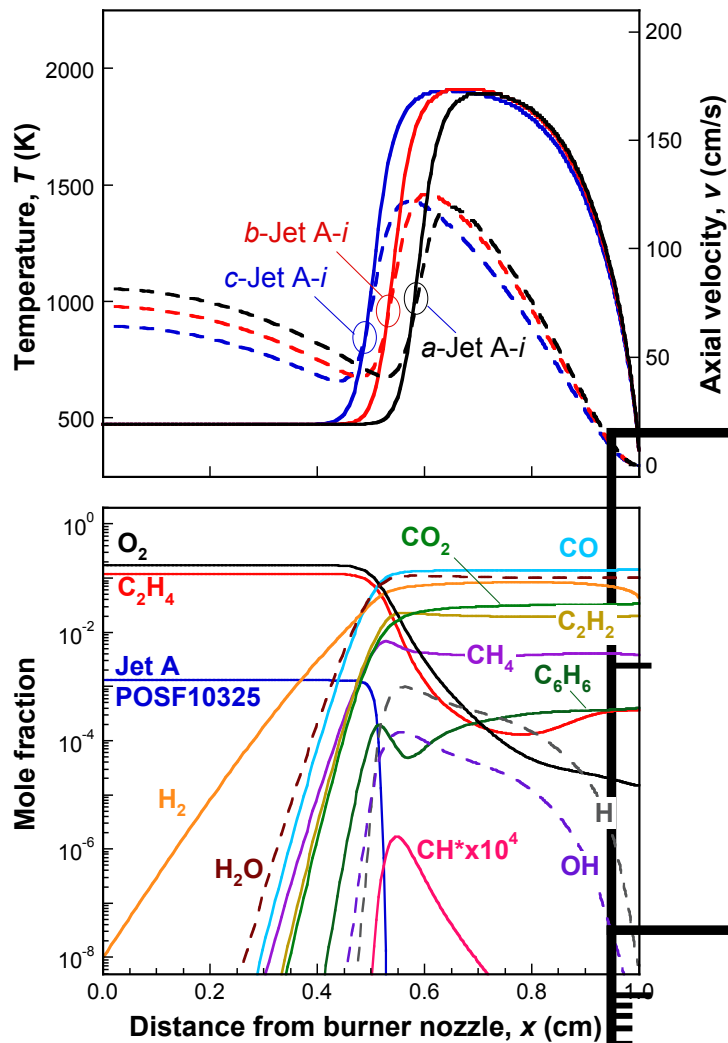
378 *3.2 Jet A versus the 2nd generation MURI surrogate in premixed stretch-stabilized flames*

379 In general, the particle size distribution functions measured for the stretch-stabilized flames can
 380 be described well by a bi-lognormal distribution [28] even though all of the PSDFs observed here
 381 are unimodal. In the form of volume distribution (nm³/cm³), we have

$$382 \frac{dV}{d\log D_m} = \sum_{i=1}^2 \frac{V_i}{\sqrt{2\pi} \log \sigma_{g,i}} \exp \left[-\frac{(\log D_m - \log \langle D_m \rangle_i)^2}{2(\log \sigma_{g,i})^2} \right],$$

383 where V is the volume fraction of the particles in the mobility diameter D_m range of $\log D_m$ to
 384 $\log D_m + d\log D_m$, V_i , $\sigma_{g,i}$ and $\langle D_m \rangle_i$ are the volume fraction, geometric standard deviation and median
 385 mobility diameter of the i^{th} particle mode, respectively. In obtaining the volume distribution, we
 386 assume that all particles are spherical such that $dV = dN(\pi D_m^3/6)$. Since the diameter D_m is the
 387 mobility diameter, the resulting volume fraction is called the mobility volume fraction hereafter.
 388 Quantitatively, this volume fraction is not identical to that measured by LII (to be discussed later).
 389 As discussed in recent works [29, 52, 53] soot particles are found to deviate from sphericity even at
 390 the early stage of growth. Hence the spherical assumption gives an upper estimate of soot volume
 391 fraction and comparisons of soot volume fraction should be considered as being semi-quantitative.

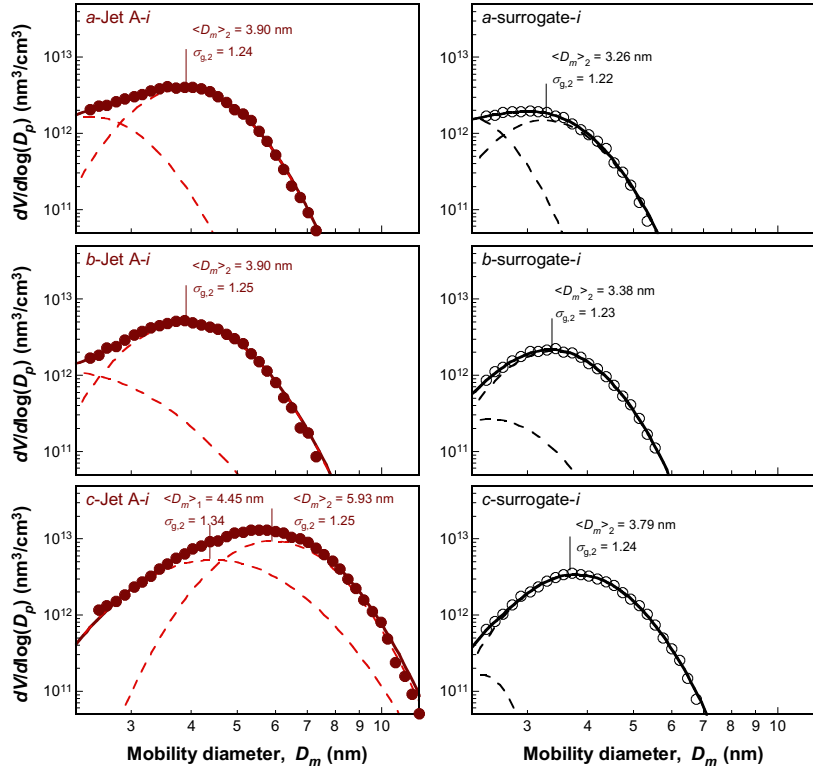
392 Fig. 4 shows the volume distribution functions measured for the ethylene flames doped with Jet A
 393 as received (the left panel) and the 2nd generation MURI surrogate (the right panel), both at 7260
 394 ppm level of dopant concentration. A similar plot is presented in Fig. S2 of the Supplementary
 395 Materials for PSDFs observed at the higher level of doping (11500 ppm). In all cases, the median
 396 diameter of the second size mode $\langle D_m \rangle_2$ increases with a decrease in the cold gas velocity from
 397 flame series *a* to *c* for a given fuel, as expected due to an increased reaction time.
 398



399
 400 **Figure 3.** Top panel: profiles of temperature (solid lines) and velocity (dashed lines) computed for the
 401 premixed stretch-stabilized flames (the Jet A-*i* series); bottom panel: profiles of species mole fraction for the
 402 *c*-Jet A-*i* flame (see Table 1 for the flame conditions).
 403
 404

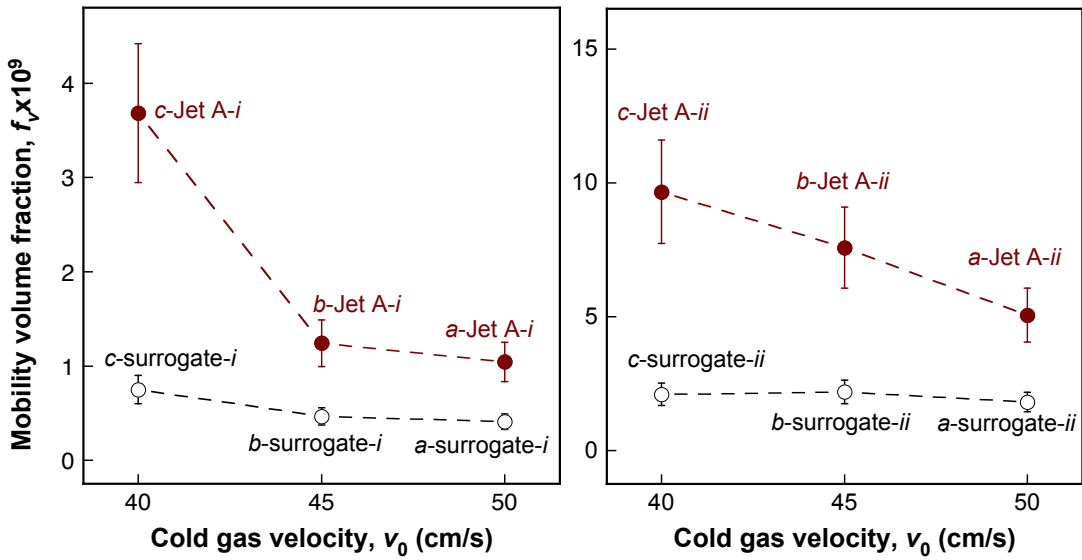
405 The soot produced from the surrogate is notably lower than from Jet A under comparable
406 conditions, both in the number density and median diameter of the particles. For comparison, in
407 the *c* series of flames (39.7 cm/s cold gas velocity) the median diameter of the second size mode is
408 5.93 nm with Jet A doping and 3.79 nm with the surrogate. Fig. 5 presents the comparisons of the
409 soot volume fraction (f_v) obtained by integrating the respective PSDFs of Fig. 4. It is seen that Jet A
410 produces two to three times more nascent soot than the MURI surrogate at the high gas velocities
411 (series *a* and *b*), and a four-fold increase of nascent soot at the lower end of the gas velocity tested
412 (series *c*). The levels of discrepancy in f_v between Jet A and the MURI surrogate are similar at the
413 higher doping of 11500 ppm. Moreover, the influence of cold gas velocity on surrogate volume
414 fraction is less evident than on Jet A. Since in these premixed flames mostly nucleation is probed,
415 the surrogate containing just 1-ring aromatics does not contribute to stronger nucleation as seen for
416 Jet fuel containing multi-ring aromatics, thus resulting in producing a lower amount of soot. The
417 evidence presented here is a clear indication that matching the TSI of a jet fuel, among its other
418 properties, does not guarantee the surrogate fuel to reproduce the real-fuel sooting tendency. Since
419 the PSDFs observed here are all for nascent soot, the difference is attributable to the greater
420 nucleation tendency of the jet fuel than its surrogate.

421
422



423
424
425
426
427

Figure 4. Comparison of mobility volume distributions of nascent soot in three series of flames, comparing the sooting properties of Jet A as received with those of the 2nd generation MURI surrogate [23]. Symbols are experimental data averaged over three runs for each case; solid lines are bi-lognormal fits to the data; dashed lines are the respective first and second terms of the lognormal function.



428
429
430
431
432
433
434

Figure 5. Comparison of mobility volume fraction of nascent soot formed in the stretch-stabilized flame doped with Jet A (as received) and 2nd generation MURI surrogate. Left panel: 7260 ppm (mass) liquid fuel doping; right panel: 11500 ppm (mass) liquid fuel doping. Symbols are experimental data; lines are drawn to guide the eyes. The PSDFs at 11500 ppm (mass) liquid fuel doping is shown in Fig. S2 of the Supplementary Materials.

435 *3.3 Distillation curve and distillate fraction properties*

436 To isolate and explore the effect of heavier aromatic compounds on soot formation and growth,
 437 Jet A was distilled into several distillate volume fractions. Soot measurements were then made for
 438 selected fractions. Properties of Jet A and its distillates from the lightest fraction (0-60 %) to the
 439 heaviest fractions (95-100 % and 98.75-100%) and the average kettle temperatures for each distillate
 440 fraction are reported in Table 4. The variations of the mass density as a function of T_k and the
 441 distillation curve are presented in Fig. 6. The distillation curve reported by Lovestead Ref. [4] is also
 442 included in the figure, showing that the current distillation procedure reproduces the earlier study
 443 completely. The current distillation curve extends into the heavy molecular weight range, from 90 to
 444 100 %. As seen in Fig. 6, T_k rises sharply in the last 10% of the distillate fraction, reaching 360 °C
 445 for the 98.75-100% fraction. Although the temperature of this heaviest fraction falls between the
 446 boiling points of phenanthrene and pyrene, the fact that the estimated H/C ratio remains close to
 447 1.9 suggests that the compounds in that fraction remain to be mostly saturated hydrocarbon species,
 448 and that polycyclic aromatics of three rings and larger are absent.

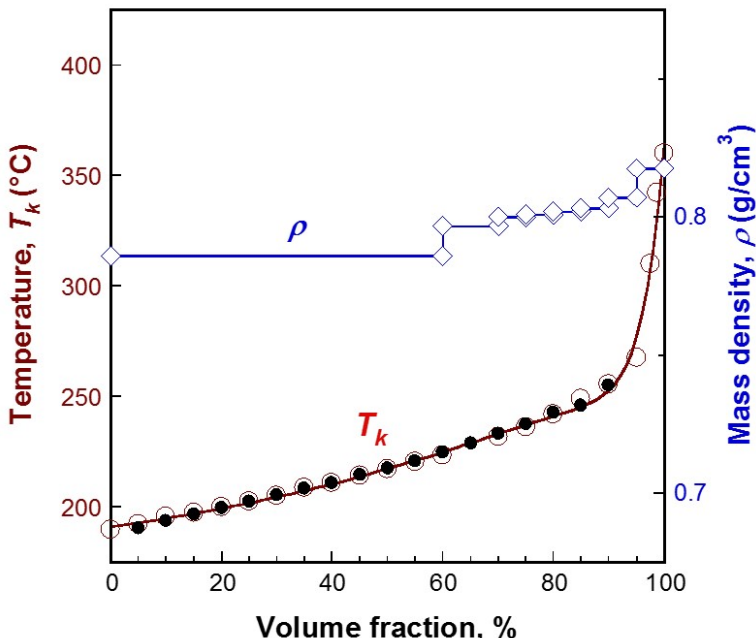
449

450 **Table 4.** Properties of Jet A (POSF 10325) and its distillate fractions.

Distillate vol. fraction (%)	Density ^a (g/cm ³)	MW ^b (g/mol)	H/C ratio ^b	T_k (°C) ^c
As received	0.803	158.6	1.91	-
0-60	0.786	153.5	1.97	223.3
60-70	0.797	156.7	1.93	231.8
70-75	0.800	157.6	1.92	236.1
75-80	0.801	157.9	1.92	241.8
80-85	0.802	158.3	1.91	248.8
85-90	0.803	158.6	1.91	255.5
90-95	0.807	159.8	1.90	267.6
95-100	0.818	163.1	1.88	
95-97.5	0.816	162.7	1.88	310.1
97.5-98.75	0.823	164.9	1.87	341.9
98.75-100	0.824	165.1	1.87	360

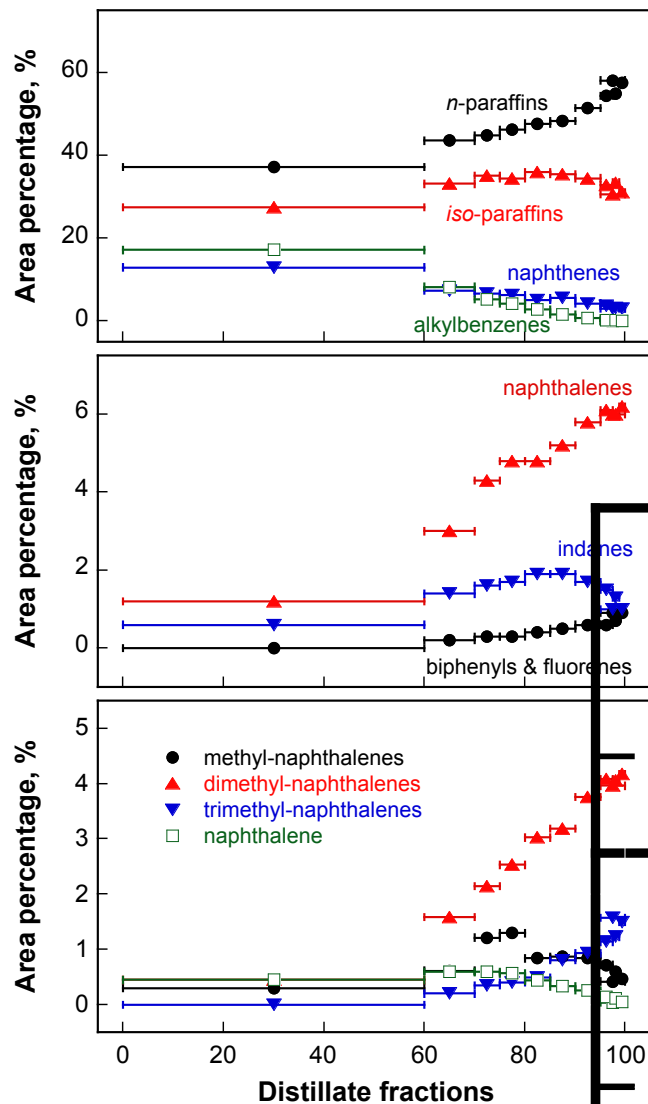
451 ^a The density of Jet A calculated from the density values measured for the
 452 distillate fractions is 0.793 g/cm³, which is 1.26% lower than that of the Jet A
 453 as received. ^b The mean molecular weight and H/C ratio are empirically
 454 estimated (see section 2.1) ^c 1-standard deviation is 0.6 °C.

455
 456



457
 458 **Figure 6.** Distillation curve (open symbols: this work, filled symbols: Lovestead et al. [4]) and mass density
 459 measured for Jet A (POSF10325). Symbols are experimental data; lines are drawn to guide the eyes.
 460

461 The above results are consistent with the GC-MS measurements made on the distillate fractions
 462 (see section S2 of the Supplementary Materials). They show that in the highest-boiling point
 463 fractions, the compounds relevant to enhanced soot nucleation are probably alkylated naphthalenes,
 464 and to a minor extent, alkylated biphenyls and fluorenes. As shown in Fig. 7, the fraction of alkyl
 465 benzenes decreases across the entire distillation curve, and the increase of *n*-paraffin and *iso*-paraffin
 466 contents is less significant than the increases in indanes, tetralins, and naphthalenes. The largest
 467 aromatic compounds were naphthalenes with up to four methyl sidechains. Within the 90-100%
 468 fraction the amount of naphthalenes with two and three additional carbons (e.g. dimethyl- and
 469 trimethyl-naphthalenes) increases while non-substituted naphthalene and methylnaphthalenes
 470 decreases. Hence, the highest-boiling point fractions are two-ring compounds but polycyclic
 471 aromatic hydrocarbons of three rings and larger are absent.



472

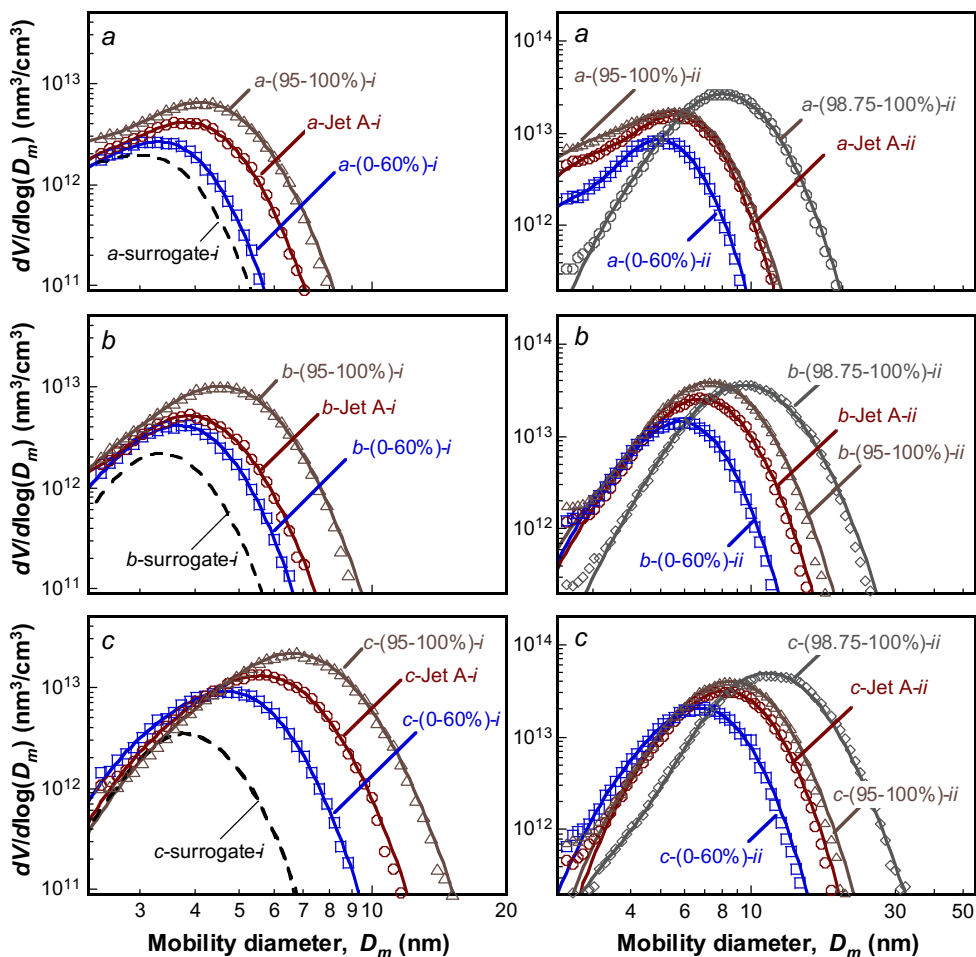
473 **Figure 7.** Area percentages as determined from GC-MS characterization of the various distillate fractions of
 474 the Jet A fuel.

475

476 3.4 Variation of soot formation from different distillate fractions in stretch-stabilized flames

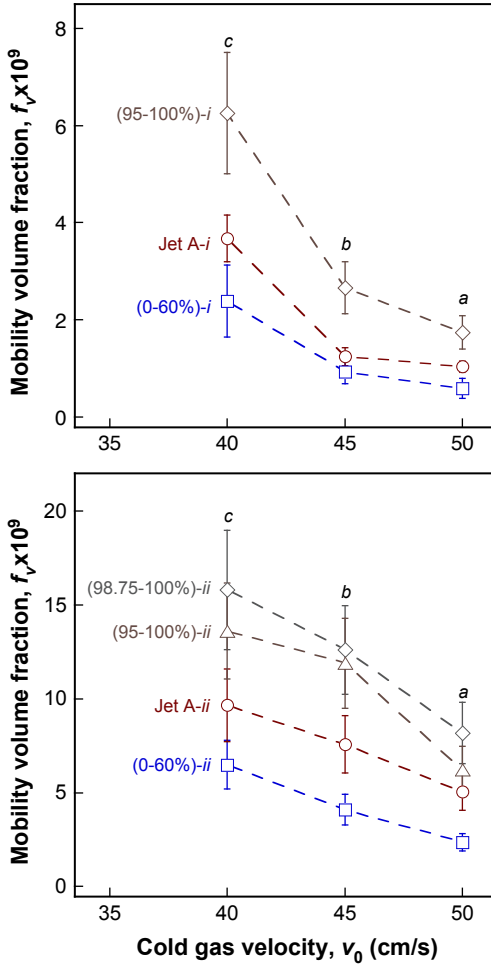
477 The PSDFs observed for the various distillate fractions are compared to those of the parent Jet
 478 A in Fig. 8. The particles measured are all nascent soot having median mobility diameter smaller
 479 than 15 nm. It is seen that the different distillate fractions do soot differently. Under all equal
 480 conditions, the heavier fraction causes stronger nucleation and produces larger particles than the
 481 light fraction in all flame series tested. Also included in Fig. 8 are the PSDFs observed for the MURI
 482 surrogate at the lower level of fuel doping. Clearly, the soot produced from the surrogate is lower
 483 even than the 0-60% distillate fraction of the Jet A.

484



485

486 **Figure 8.** Comparison of mobility volume distributions of nascent soot in series *a*, *b* and *c* flames doped with
 487 7200 ppm by mass (left panel) and 11500 ppm by mass (right panel) of Jet A as received, and its 0-60%, 95-
 488 100% and 98.7-100% distillate fractions. Symbols are experimental data averaged over three runs for each
 489 case; lines are bi-lognormal fits to the data. The dashed lines in the left panel are mobility distributions of the
 490 2nd generation MURI surrogate for comparable conditions.



491
492 **Figure 9.** Mobility volume fraction of nascent soot measured at the stagnation surface in host flames doped
493 with 7200 ppm (mass) (top panel) and 11500 ppm (bottom panel) of Jet A as received (0-100%), and its 0-
494 60% and 95-100% distillate fractions. The bottom panel also includes the data taken for the 98.75-100%
495 distillate fraction of Jet A. Symbols are experimental data; lines are drawn to guide the eyes.
496

497 The corresponding volume fraction data are presented in Fig. 9. As expected, the volume
498 fraction in flames doped with Jet A (as received) lies between those from the 0-60% and 95-100%
499 distillate fractions. As discussed before, the flames tested at a given level of fuel doping have nearly
500 the same equivalence and H/C ratio. The difference observed in the soot volume fraction can only
501 be the result of differences in the molecular components of the fuels. Keep in mind that in these
502 premixed stretch-stabilized flames, soot nucleates behind the flame with respect to the unburned
503 mixture flow. Fuel components must pass through the flame layer before nucleation can occur; most
504 of the heavy components must have been oxidized or undergo significant decomposition in the
505 premixed flame. Even so, the difference in soot production is significant. It illustrates the role of the

506 heavy or high-boiling point components in promoting soot nucleation. In particular, the fact that the
507 2nd generation MURI surrogate does not reproduce soot nucleation and early soot growth rate may
508 be explained by the lack of two-ring compounds in its formulation – an issue already suggested in
509 some of the earlier studies (see, e.g. [24, 25]).

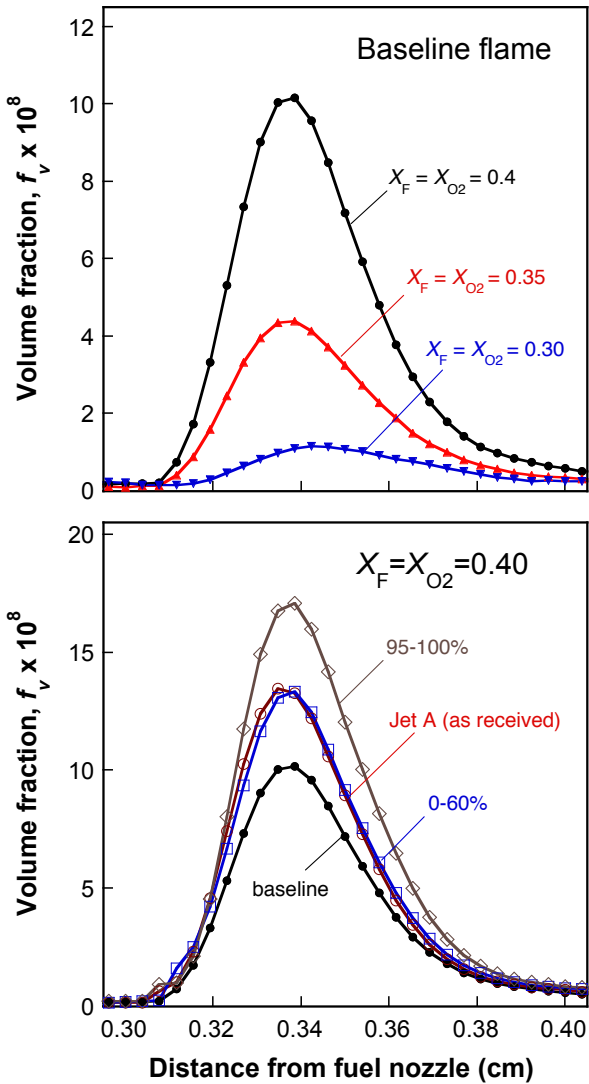
510
511

512 *3.5 Counterflow diffusion flames*

513 The top panel of Fig. 10 presents the spatially-resolved soot volume fraction profiles along the
514 centerline of three undoped, baseline counterflow diffusion ethylene flames. It is seen that the
515 overall soot layer thickness is similar and the soot volume fractions all peak around 0.34 cm from
516 the fuel nozzle. Fig. 10 shows that both the total soot yield and the maximum soot volume fraction
517 along the centerline, $f_{v,\max}$, increases with increasing X_F and X_{O_2} . Jet A or its distillate fractions was
518 doped after a baseline ethylene flame was established. In order to ensure that the doped flame
519 reached steady state, the LII signal was monitored from the moment of liquid fuel injection [54].
520 The signal increases sharply within the first two minutes and reaches a constant value after 14 min.
521 The LII data were taken at 20 min after the moment of liquid fuel injection.

522 In the bottom panel of Fig. 10, soot volume fraction profiles are shown for the baseline flame at
523 $X_F = X_{O_2} = 0.40$ and the corresponding doped flames. It can be seen that the profile thicknesses are
524 again similar to each other among the flames studied, indicating that the level of dopant does not
525 affect the flame structure significantly. When doped with Jet A, the peak soot volume fraction
526 increases by about 30% from the undoped flame. The volume fraction profile in the flame doped
527 with the 0-60% distillate fraction is almost the same as that of Jet A, suggesting that the nucleation
528 and growth of soot are driven as much by the lower-boiling point components as the higher-boiling
529 point components for the counterflow flame tested. For the same reason, the effect of the high-
530 boiling point fraction on soot production is relatively mild. Doping with the 95-100% fraction
531 causes the peak volume fraction to increase merely 30% compared to doping with Jet A as received.

532
533

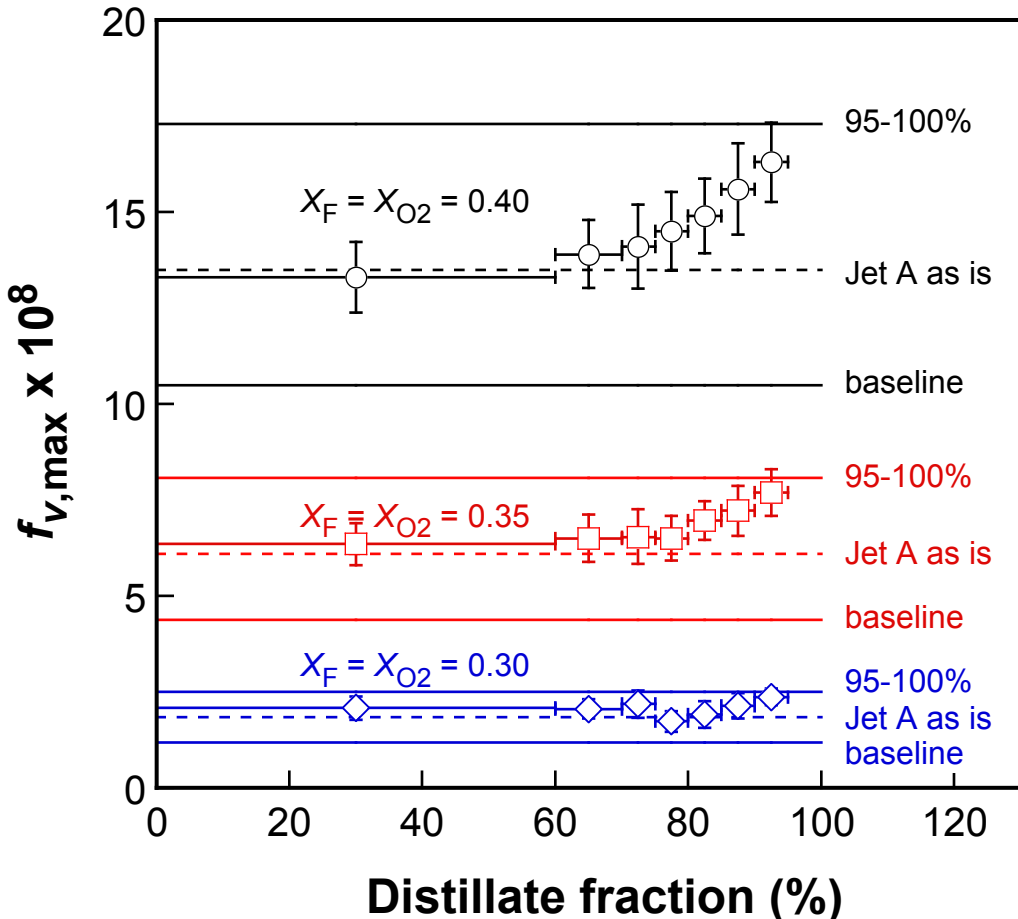


534

535 **Figure 10.** Soot volume fraction profiles along the centerline. Top panel: baseline, undoped flames; bottom
 536 panel: flames at $X_F = X_{O_2} = 0.40$ doped with Jet A as received (0-100%), and its 0-60% and 95-100%
 537 distillate fractions. Symbols are experimental data; lines are drawn to guide the eyes.

538

539 Fig. 11 plots the variation of $f_{v,\max}$ as function of the volume percentage of the various distillate
 540 fractions in three baseline flames tested. Doping of Jet A or its distillates at 2000 ppm (mol) level
 541 generally leads to an increase in $f_{v,\max}$, but the impact of the high-boiling point components on soot
 542 production is gradual and mild. For the baseline flame at the lowest ethylene and oxygen
 543 concentration, i.e., $X_F = X_{O_2} = 0.30$, the variation of the maximum soot volume fraction is small and
 544 probably within the experimental uncertainty of the data across the distillation fractions tested.



545
546
547
548
549
550
551

Figure 11. Variation of the maximum soot volume fractions measured for different distillation fractions in three baseline flames. The horizontal lines mark the maximum volume fractions of the baseline flame, with additions of Jet A as received and the 95-100% fraction. The x-axis data value represents the center point of the distillate volume fraction range; its horizontal “error” bar represents the range of the respective distillate volume fraction.

552 *3.6 Coflow diffusion flames*

553 In section 3.2, we used a series of premixed, stretch-stabilized flames to show that TSI is an
554 ambiguous indicator of the sooting property of a jet fuel. In other words, matching the TSI and
555 H/C ratio of a jet fuel does not guarantee that the surrogate fuel will reproduce the real-fuel sooting
556 tendency. To shed light on this issue, we report here the results obtained in coflow diffusion flames
557 with the expectation that the 2nd generation MURI surrogate reproduces the sooting properties of
558 the jet fuel tested since TSI is measured in diffusion flames and therefore involves the same stages
559 of soot production present in coflow diffusion flames. Indeed, Figure S1 of the paper of Zhang et

560 al. [55] shows that the soot volume fraction profiles of the 2nd generation MURI surrogate is very
561 close to those of Jet-A POSF 4658. Moreover, as discussed in Hura and Glassman [56], the smoke
562 point is determined by the competing processes of soot nucleation and growth and soot oxidation.
563 Therefore TSI should be used with some caution as it measures the competing effects of two spatially
564 separate processes. For this reason, probing the internal structure of the soot profile in a coflow flame
565 is necessary to understand the sooting propensity of a fuel.

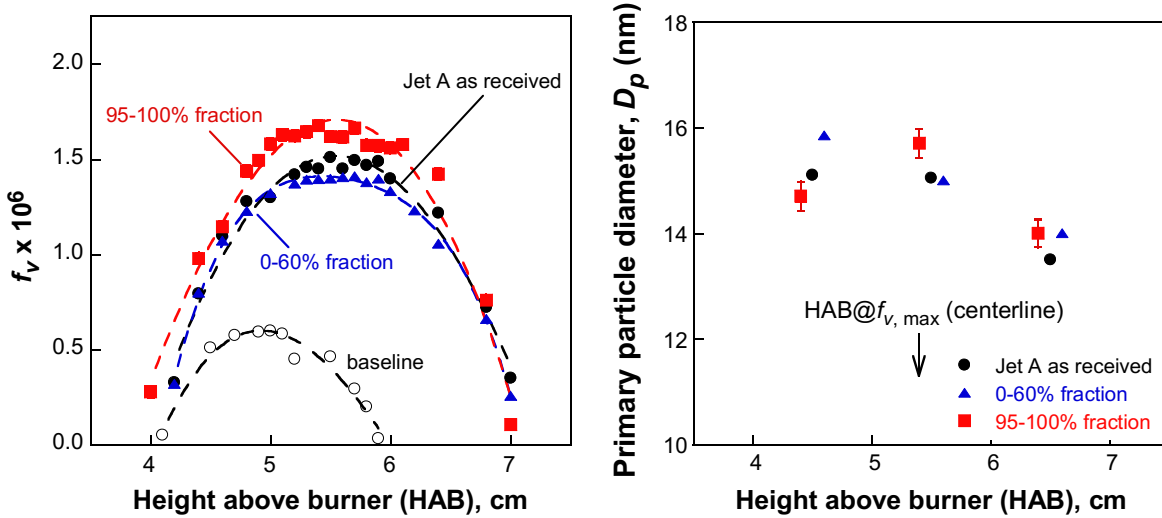
566 Images of the four coflow flames tested are shown in Fig. S3 of the Supplementary Materials.
567 Parameters of the flames are listed in Table 3. All doped flames exhibit similar heights and the
568 baseline flame is about 0.5 cm shorter. The onset of the yellow luminosity of the baseline, undoped
569 flame was observed to be at higher HABs than those of the doped flames. Since the mass flow rates
570 of the fuel(s) are nearly equal among the doped and undoped flames (see, Table 3), the HAB
571 difference at the onset of luminosity indicates that the jet fuel and its distillates do generate more
572 soot than ethylene.

573 Centerline soot volume fraction (f_s) profiles shown in the left panel of Fig. 12 provide a
574 quantitative comparison of the relative sooting tendency of the four flames. The doped flames (Jet A
575 as is, and the 0-60% and 95-100% distillate fractions) have significantly higher soot volume fraction
576 compared to the base flame, highlighting the importance of fuel structure and composition on soot
577 formation. The significant difference between the doped and baseline flames can be explained by an
578 earlier soot nucleation and higher particle growth rates as a result of the presence of aromatics in the
579 fuel. Soot nucleation occurs at lower heights in flames when aromatic compounds already exist in
580 the fuel stream. Similar phenomenon was observed by Zhang et al. [57, 58], who studied the
581 addition of *n*-propylbenzene into *n*-dodecane laminar coflow diffusion flame.

582 Soot concentration profiles of the jet fuel as received are not significantly different from its
583 distillate fractions. The volume fraction from the flame doped with the 95-100% distillate fraction is
584 moderately higher than that of the jet fuel as received, which in turn, is higher than that from the 0-
585 60% fraction. It is likely that this reduced sensitivity toward the distillate fraction is caused by the
586 relatively longer periods of particle growth (more than 100 ms for the flame tested) over particle

587 nucleation than in premixed flames. The dominance of surface growth (as opposed to coagulation)
 588 is consistent with the observation that the primary particle diameters are all nearly equal among the
 589 three flames studied, as illustrated in the right panel of Fig. 12 for measurements on the centerline as
 590 well as in the wings as shown in Fig. S5 of the Supplementary Materials.

591



592

593 **Figure 12.** Centerline soot volume fraction (left panel) and the particle diameter of primary particles (right
 594 panel) measured along the centerline of the coflow diffusion flame. Symbols are experimental data. Lines in
 595 the left panel are drawn to guide the eyes. The error bars represent one standard deviation of the sample size
 596 of around 500 counts. The error bars are discussed in section 2.4 and for the volume fraction they are smaller
 597 than the symbols.

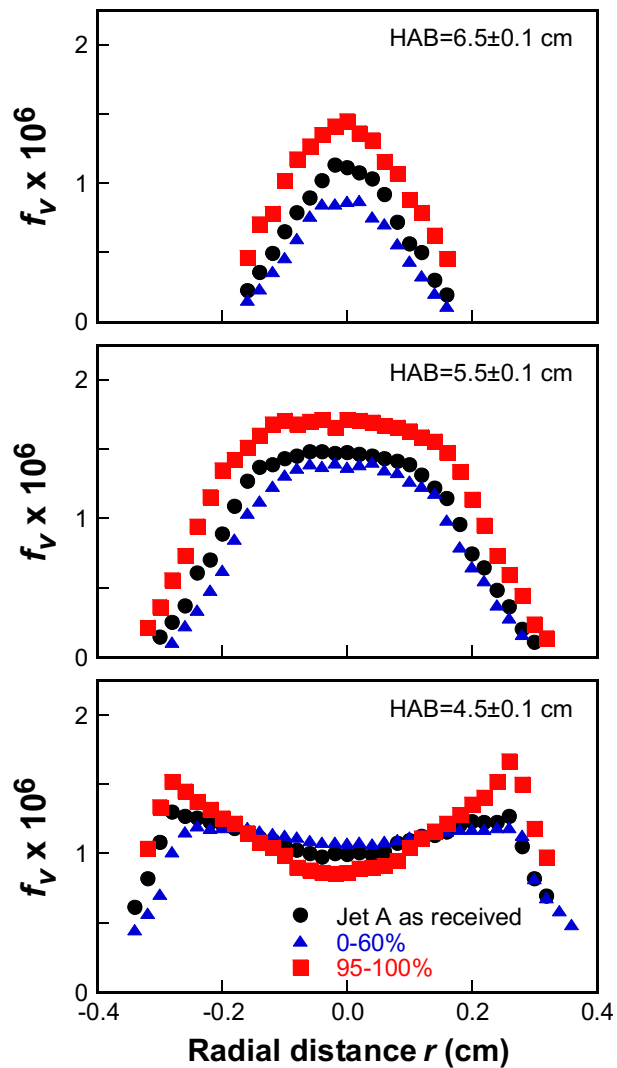
598 Calculating the primary particle number density from the measured soot volume fraction and
 599 primary particle diameter reveals that the flame doped with the 95-100% distillate fraction generally
 600 has a higher particle number density at the height of maximum f_v , while those of the jet fuel as
 601 received and its 0-60% fraction are similar (see, Fig. S6 of the Supplementary Materials).

602 Fig. 13 shows the evolution of radial f_v profiles at three characteristic flame heights. Radially, the
 603 peak soot appears in the wings at $HAB = 4.5 \pm 0.1$ cm, or 1.0 cm below the height at which the
 604 centerline soot f_v peaks. The peak soot volume fraction in the wings migrates and converges toward
 605 the centerline as HAB increases. The centerline f_v peaks at around 5.5 cm for all doped flames (the
 606 middle panel of Fig. 13), and eventually decreases in the peak value and more notably, in the wings
 607 (*cf.* the middle and top panels of Fig. 13). Again, in all cases, the effect of the distillate fraction on

608 soot production is consistently observed, from the wings to the centerline of the flame, but like the
 609 counterflow diffusion flames tested, the effect is not as significant as one would observe in the
 610 premixed stretch-stabilized flames. Moreover since soot volume fraction is less than 2 ppm,
 611 aggregates concentration is expected to be low and shielding and bridging effects can be neglected.

612

613



614

615 **Figure 13.** Radial soot volume fraction profiles measured at three characteristic flame heights. $HAB =$
 616 5.5 ± 0.1 cm corresponds to the maximum centerline volume fraction for each of the flames. The error bars
 617 are smaller than the symbols.

618

619 **4. Discussion**

620 Aside from the fact that the data presented above are useful to the rational development of a
621 reaction model for soot formation, there are several important findings that we can summarize
622 concerning the sooting processes of real jet fuel. To start, evidence from literature [9-11] and the
623 current study in premixed flames all suggest that one or more two-ring aromatic compounds must
624 be considered in a fuel surrogate for it to reproduce the sooting properties. The results of the
625 current study firmly attribute this to the presence of two-ring aromatic compounds in the tail end of
626 the distillation curve. This evidence suggests that matching the sooting properties in any laboratory
627 flames in which the liquid fuel is pre-vaporized may not truthfully mimic the real combustion
628 situation in which the fuel is injected into a combustor as a spray. Preferential vaporization
629 according to the different boiling points of fuel components can lead to the formation of pockets
630 rich in high-molecular weight, multi-ring species.

631 The fuel components in the tail end of the distillation curve impact soot formation primarily
632 through enhanced particle nucleation, as evidenced by the observations made in the premixed
633 stretch-stabilized flames. For flames in which the soot yield is not as sensitive to nucleation, such as
634 the counterflow and coflow diffusion flames studied herein, this effect is insignificant. Yet, the
635 observation that soot formation can be sensitive to the distillation fraction poses another challenge
636 in modeling soot formation in real fuels. Currently, it is unclear whether this effect must be
637 accounted for in modeling soot formation in real engines. Suffice it to note that the surrogate fuel
638 approach cannot account for the impact of preferential evaporation and its effect on soot formation
639 and simultaneously make useful predictions for the heat release and flame extinction.

640 One of the interesting implications of the present findings is that to reduce soot production
641 from real jet fuels, perhaps the most efficient approach is to place tighter constraints on the
642 distillation process. As seen in Fig. 6, the temperature of the distillation curve shoots up above 90%
643 of the volume fraction. It is in this fraction we expect to see drastically increased presence of multi-
644 ring compounds. Excluding these compounds by keeping the upper limit of the distillation
645 temperature to 250 °C would remove a large fraction of the multi-ring aromatic compounds and

646 thus lowering the fuel sooting propensity. Of course, whether such a change can be made in the
647 petroleum refining process, the cost associated with it and possible changes in other fuel properties
648 remain to be open questions.

649 Lastly, we note that flames directly burning a certain distillate fraction would give a more direct
650 measure for the distillate fraction dependent sooting property. Such experiments are difficult to
651 carry, however, because the need for a large amount of fuel and the difficulties associated with the
652 vaporization of high boiling point fractions in the experiment. We believe that the use of the
653 distillate fraction in ethylene is as close to the real engine combustion condition as any lab
654 experiments can get close to. The principle reason is that in the flame front jet fuels decompose to
655 mainly ethylene [2,38], and as such the high-molecular weight fraction of the fuel mixed with
656 ethylene does mimic the mixture properties under real combustion situation to a large extent. In any
657 case, the mixture conditions in the flames probed here are substantially closer to those in real
658 engines than sooting property experiments in which methane is used as the base fuel. In that case,
659 the overall H/C ratio and hence the thermodynamic and chemical kinetic conditions are far different
660 from those in engines.

661

662 5. Conclusions

663 The sooting properties of a typical Jet A (POSF 10325) were studied in detail across three flame
664 platforms: the premixed stretch-stabilized flame, and counterflow and coflow diffusion flames, with
665 an emphasis on the role of different distillate fraction of the fuel in soot formation. In all cases
666 studied, the jet fuel or one of its distillate fractions is doped into baseline flames burning ethylene.
667 The particle size distribution functions were also collected for the 2nd generation MURI surrogate in
668 the premixed stretch-stabilized flame under comparable conditions. The results indicate:

669 1) The 2nd generation MURI surrogate does not reproduce soot nucleation in the premixed stretch-
670 stabilized flame well. The cause is likely to be the lack of a two-ring compound in its
671 formulation;

672 2) The tail end of the Jet A distillation curve is accompanied with an increased level of two-ring
673 aromatic compounds (e.g., alkylated naphthalenes, alkylated biphenyls, and fluorenes), which
674 drastically promote soot nucleation in the premixed stretch-stabilized flames;
675 3) In the diffusion flames studied, however, the effect just discussed is minor as soot production in
676 these flames is more sensitive to soot surface growth than particle nucleation.

677 Taken together, the experimental measurements discussed herein are expected to be useful in
678 formulating a rational strategy for modeling soot formation from real jet fuels. Such a strategy may
679 have to consider the role of fuel evaporation as a necessary component of a predictive soot model.

680

681 **Acknowledgements**

682 The work at Stanford was supported by the National Aeronautics and Space Administration
683 (NASA grant number NNX15AV05A). MRK was supported by NSERC Michael Smith Foreign
684 Study award as well as BioFuelNet Canada exchange fund during his time at Stanford. Work at the
685 University of Toronto was supported by NSERC and BioFuelNet Canada.

686

References

- [1] Colket M, Heyne J, Rumizen M, Gupta M, Edwards T, Roquemore WM, et al. Overview of the National Jet Fuels Combustion Program. *AIAA J* 2017; 55:1087-104.
- [2] Xu R, Wang K, Banerjee S, Shao J, Parise T, Zhu Y, et al. A Physics-based approach to modeling real-fuel combustion chemistry - II. Reaction kinetic models of jet and rocket fuels. *Combust Flame* 2018; 193: 520-537.
- [3] Council CR. *Handbook of aviation fuel properties*. The Council; 1983.
- [4] Lovestead TM, Burger JL, Schneider N, Bruno TJ. Comprehensive Assessment of Composition and Thermochemical Variability by High Resolution GC/QToF-MS and the Advanced Distillation-Curve Method as a Basis of Comparison for Reference Fuel Development. *Energy Fuels* 2016; 30(12):10029-44.
- [5] Smith BL, Bruno TJ. Improvements in the measurement of distillation curves. 4. Application to the aviation turbine fuel Jet-A. *Ind Eng Chem Res* 2007; 46(1):310-20.
- [6] Burger JL, Bruno TJ. Application of the advanced distillation curve method to the variability of jet fuels. *Energy Fuels* 2012; 26(6):3661-71.
- [7] Moss J, Aksit I. Modelling soot formation in a laminar diffusion flame burning a surrogate kerosene fuel. *Proc Combust Inst* 2007; 31(2):3139-46.
- [8] Saffaripour M, Zabeti P, Kholghy M, Thomson MJ. An experimental comparison of the sooting behavior of synthetic jet fuels. *Energy Fuels* 2011; 25(12):5584-93.
- [9] Saffaripour M, Kholghy M, Dworkin S, Thomson MJ. A numerical and experimental study of soot formation in a laminar coflow diffusion flame of a jet A-1 surrogate. *Proc Combust Inst* 2013; 34(1):1057-65.
- [10] Saffaripour M, Veshkini A, Kholghy M, Thomson MJ. Experimental investigation and detailed modeling of soot aggregate formation and size distribution in laminar coflow diffusion flames of Jet A-1, a synthetic kerosene, and n-decane. *Combust Flame* 2014; 161(3):848-63.
- [11] Witkowski D, Kondo K, Vishwanathan G, Rothamer D. Evaluation of the sooting properties of real fuels and their commonly used surrogates in a laminar co-flow diffusion flame. *Combust Flame* 2013; 160(6):1129-41.
- [12] Aksit I, Moss J. Model fuels to reproduce the sooting behaviour of aviation kerosene. *Fuel* 2005; 84(2-3):239-45.
- [13] Mouis AG, Litzinger TA, Wang Y, Iyer V, Iyer S, Linevsky M, et al. Effects of a JP-8 surrogate and its components on soot in laminar, N 2-diluted ethylene co-flow diffusion flames from 1 to 5atm. *Combust Flame* 2015; 162(5):1987-95.

[14] Jahangirian S, McEnally CS, Gomez A. Experimental study of ethylene counterflow diffusion flames perturbed by trace amounts of jet fuel and jet fuel surrogates under incipiently sooting conditions. *Combust Flame* 2009; 156(9):1799-809.

[15] Bufferand H, Tosatto L, La Mantia B, Smooke M, Gomez A. Experimental and computational study of methane counterflow diffusion flames perturbed by trace amounts of either jet fuel or a 6-component surrogate under non-sooting conditions. *Combust Flame* 2009; 156(8):1594-603.

[16] Tosatto L, La Mantia B, Bufferand H, Duchaine P, Gomez A. Chemical structure of a methane counterflow diffusion flame perturbed with the addition of either JP-8 or a jet fuel surrogate. *Proc Combust Inst* 2009; 32(1):1319-26.

[17] Honnet S, Seshadri K, Niemann U, Peters N. A surrogate fuel for kerosene. *Proc Combust Inst* 2009; 32(1):485-92.

[18] Carbone F, Gomez A. Chemical interactions between 1, 2, 4-trimethylbenzene and n-decane in doped counterflow gaseous diffusion flames. *Proc Combust Inst* 2015; 35(1):761-9.

[19] Dagaut P, Gaïl S. Chemical kinetic study of the effect of a biofuel additive on Jet-A1 combustion. *J Phys Chem A* 2007; 111(19):3992-4000.

[20] Dooley S, Won SH, Chaos M, Heyne J, Ju Y, Dryer FL, et al. A jet fuel surrogate formulated by real fuel properties. *Combust Flame* 2010; 157(12):2333-9.

[21] Lemaire R, Therssen E, Pauwels J, Desgroux P. Experimental comparison of soot formation in turbulent flames of kerosene and surrogate model fuels. In: Bockhorn H, D'Anna A, Sarofim A, Wang H, Eds. *Combustion Generated Fine Carbonaceous Particles: Proceedings of an International Workshop held in Villa Orlandi, Anacapri*. Karlsruhe: KIT Scientific Publishing; 2009, p. 619-36.

[22] Dryer FL. Chemical kinetic and combustion characteristics of transportation fuels. *Proc Combust Inst* 2015; 35(1):117-44.

[23] Dooley S, Won SH, Heyne J, Farouk TI, Ju Y, Dryer FL, et al. The experimental evaluation of a methodology for surrogate fuel formulation to emulate gas phase combustion kinetic phenomena. *Combust Flame* 2012; 159(4):1444-66.

[24] Yang Y, Boehman AL, Santoro RJ. A study of jet fuel sooting tendency using the threshold sooting index (TSI) model. *Combust Flame* 2007; 149(1-2):191-205.

[25] Das DD, McEnally CS, Kwan TA, Zimmerman JB, Cannella WJ, Mueller CJ, et al. Sooting tendencies of diesel fuels, jet fuels, and their surrogates in diffusion flames. *Fuel* 2017; 197:445-58.

[26] Smith BL, Ott LS, Bruno TJ. Composition-explicit distillation curves of commercial biodiesel fuels: Comparison of petroleum-derived fuel with B20 and B100. *Ind Eng Chem Res* 2008; 47(16):5832-40.

[27] Commodo M, Wong O, Fabris I, Groth CP, Gölde ÖL. Spectroscopic study of aviation jet fuel thermal oxidative stability. *Energy Fuels* 2010; 24(12):6437-41.

[28] Camacho J, Singh AV, Wang W, Shan R, Yapp EK, Chen D, et al. Soot particle size distributions in premixed stretch-stabilized flat ethylene–oxyge flames. *Proc Combust Inst* 2017; 36(1):1001-9.

[29] Camacho J, Liu C, Gu C, Lin H, Huang Z, Tang Q, et al. Mobility size and mass of nascent soot particles in a benchmark premixed ethylene flame. *Combust Flame* 2015; 162(10):3810-22.

[30] Abid AD, Camacho J, Sheen DA, Wang H. Quantitative measurement of soot particle size distribution in premixed flames—the burner-stabilized stagnation flame approach. *Combust Flame* 2009; 156(10):1862-70.

[31] Li Z, Wang H. Drag force, diffusion coefficient, and electric mobility of small particles. I. Theory applicable to the free-molecule regime. *Phys Rev E* 2003; 68(6):061206.

[32] Singh J, Patterson RI, Kraft M, Wang H. Numerical simulation and sensitivity analysis of detailed soot particle size distribution in laminar premixed ethylene flames. *Combust Flame* 2006; 145(1-2):117-27.

[33] Li Z, Wang H. Drag force, diffusion coefficient, and electric mobility of small particles. II. Application. *Phys Rev E* 2003; 68(6):061207.

[34] Li Z, Wang H. Comment on “Phenomenological description of mobility of nm-and sub-nm-sized charged aerosol particles in electric field” by Shandakov, SD, Nasibulin, AG and Kauppinen, EI. *J Aerosol Sci* 2006; 37(1):111-4.

[35] Wang, H. Formation of nascent soot and other condensed-phase materials in flames. *Proc Combust Inst* 2011; 33: 41-67.

[36] Banerjee S, Tangko R, Sheen DA, Wang H, Bowman CT. An experimental and kinetic modeling study of n-dodecane pyrolysis and oxidation. *Combust Flame* 2016; 163:12-30.

[37] Cuoci A, Frassoldati A, Faravelli T, Ranzi E. OpenSMOKE++: An object-oriented framework for the numerical modeling of reactive systems with detailed kinetic mechanisms. *Comput Phys Commun* 2015; 192:237-64.

[38] Wang H, Xu R, Wang K, Bowman CT, Davidson DF, Hanson RK, et al. A Physics-based approach to modeling real-fuel combustion chemistry - I. Evidence from experiments, and thermodynamic, chemical kinetic and statistical considerations. *Combust Flame* 2018; 193: 502-519.

[39] Singh P, Hui X, Sung C-J. Soot formation in non-premixed counterflow flames of butane and butanol isomers. *Combust Flame* 2016; 164:167-82.

[40] Singh P, Sung C-J. PAH formation in counterflow non-premixed flames of butane and butanol isomers. *Combust Flame* 2016; 170:91-110.

[41] Xue X, Hui X, Singh P, Sung C-J. Soot formation in non-premixed counterflow flames of conventional and alternative jet fuels. *Fuel* 2017; 210:343-51.

[42] Shaddix CR, Smyth KC. Laser-induced incandescence measurements of soot production in steady and flickering methane, propane, and ethylene diffusion flames. *Combust Flame* 1996; 107(4):418-52.

[43] Kholghy M, Afarin Y, Sediako AD, Barba J, Lapuerta M, Chu C, et al. Comparison of multiple diagnostic techniques to study soot formation and morphology in a diffusion flame. *Combust Flame* 2017; 176:567-83.

[44] Snelling DR, Thomson KA, Smallwood GJ, Gülder ÖL, Weckman E, Fraser R. Spectrally resolved measurement of flame radiation to determine soot temperature and concentration. *AIAA J* 2002; 40(9):1789-95.

[45] Nestor O, Olsen H. Numerical methods for reducing line and surface probe data. *SIAM Rev* 1960; 2(3):200-7.

[46] Thomson KA. Soot formation in annular non-premixed laminar flames of methane-air at pressures of 0.1 to 4.0 MPa. University of Waterloo; 2004.

[47] Williams TC, Shaddix C, Jensen K, Suo-Anttila J. Measurement of the dimensionless extinction coefficient of soot within laminar diffusion flames. *Int J Heat Mass Tran* 2007; 50(7-8):1616-30.

[48] Snelling DR, Liu F, Smallwood GJ, Gülder ÖL. Evaluation of the nanoscale heat and mass transfer model of LII: prediction of the excitation intensity. *Proceedings of the 34th National Heat Transfer Conference*. 2000, p. 79-87.

[49] Snelling DR, Liu F, Smallwood GJ, Gülder ÖL. Determination of the soot absorption function and thermal accommodation coefficient using low-fluence LII in a laminar coflow ethylene diffusion flame. *Combust Flame* 2004; 136(1-2):180-90.

[50] Saffaripour M, Geigle K-P, Snelling D, Smallwood G, Thomson K. Influence of rapid laser heating on the optical properties of in-flame soot. *Appl Phys B-Lasers O* 2015; 119(4):621-42.

[51] Bachalo WD, Sankar SV, Smallwood GJ, Snelling DR. Development of the laser-induced incandescence method for the reliable characterization of particulate emissions. *11th International Symposium on Applications of Laser Techniques to Fluid Mechanics*. Lisbon, Portugal; July, 2002, p. 8-111.

[52] Schenk M, Lieb S, Vieker H, Beyer A, Gölzhäuser A, Wang H, et al. Imaging nanocarbon materials: Soot particles in flames are not structurally homogeneous. *ChemPhysChem* 2013; 14(14):3248-54.

[53] Schenk M, Lieb S, Vieker H, Beyer A, Gölzhäuser A, Wang H, et al. Morphology of nascent soot in ethylene flames. *Proc Combust Inst* 2015; 35(2):1879-86.

- [54] Das DD, Cannella WJ, McEnally CS, Mueller CJ, Pfefferle LD. Two-dimensional soot volume fraction measurements in flames doped with large hydrocarbons. *Proc Combust Inst* 2017; 36(1):871-9.
- [55] Zhang T, Zhao L, Kholghy M, Thion S, Thomson MJ. Detailed investigation of soot formation from jet fuel in a diffusion flame with comprehensive and hybrid chemical mechanisms. *Proc Combust Inst* 2019; accepted.
- [56] Hura HS, Glassman I. Soot formation in diffusion flames of fuel/oxygen mixtures. *Symp (Int) Combust* 1989; 22(1):371-8.
- [57] Zhang T, Thomson MJ. A numerical study of the effects of n-propylbenzene addition to n-dodecane on soot formation in a laminar coflow diffusion flame. *Combust Flame* 2018; 190:416-31.
- [58] Zhang T, Zhao L, Thomson MJ. Effects of n-propylbenzene addition to n-dodecane on soot formation and aggregate structure in a laminar coflow diffusion flame. *Proc Combust Inst* 2017; 36(1):1339-47.